Morphology-Dependent Electrocatalytic Activity of Nanostructured Pt/C Particles from Hybrid Aerosol–Colloid Process

Ratna Balgis, Aditya F. Arif, Takahiro Mori, Takashi Ogi, and Kikuo Okuyama
Dept. of Chemical Engineering, Graduate School of Engineering, Hiroshima University, 1-4-1 Kagamiyama, Higashi-Hiroshima, Hiroshima 739-8527, Japan

Gopinathan M. Anilkumar
Research and Development Center, Noritake Co., Ltd., 300 Higashiyama, Miyoshi, Aichi 470-0293, Japan

DOI 10.1002/aic.15059
Published online October 2, 2015 in Wiley Online Library (wileyonlinelibrary.com)

An optimum nanostructure and pore size of catalyst supports is very important in achieving high catalytic performances. In this instance, we evaluated the effects of various carbon nanostructures on the catalytic performances of carbon-supported platinum (Pt/C) electrocatalysts experimentally and numerically. The Pt/C catalysts were prepared using a hybrid method involving the preparation of dense, hollow, and porous nanostructured carbon particle via aerosol spray pyrolysis followed by microwave-assisted Pt deposition. Electrochemical characterization of the catalysts showed that the porous Pt/C catalyst gave the best performance; its electrochemical surface area was much higher, more than twice than those of hollow or dense Pt/C. The effects of pore size on electrocatalysis were also studied. The results showed the importance of a balance between mesopores and macropores for effective catalysis with a high charge transfer rate. A fluid flow model showed that good oxygen transport contributed to the catalytic activity. © 2015 American Institute of Chemical Engineers *AIChE J*, 62: 440–450, 2016
Keywords: nanostructured Pt/C, pore size, catalytic activity, fluid flow model, oxygen transport

Introduction

In response to the needs of modern society and emerging environmental concerns, it is essential to develop renewable, low-cost, and environmentally friendly energy-supplying systems. Proton exchange membrane fuel cells (PEMFCs) are potential candidates, and are continuously being developed and improved.[1–5] One of the factors to be considered in the development of PEMFCs is the electrocatalyst, because it has a significant role in determining the PEMFC performance.[6,7] Innovations in electrocatalyst materials such as the introduction of various catalyst supports are the key to developing new generations of industrially applicable high-performance electrocatalysts.[8,9] Carbon nanoparticles (NPs) with high specific surface areas, such as Vulcan carbon, have been widely used as catalyst supports. They significantly reduce the required amount of Pt and improve the performance of the electrocatalyst.[10] The presence of carbon NPs may inhibit rapid agglomeration of Pt NPs under the harsh acid conditions in PEMFCs.

Carbon NPs naturally agglomerate over time. This has disadvantages in electrocatalytic applications because it reduces the amount of active Pt NP sites, inhibits gas flow through a packed catalyst, and reduces the durability of the electrocatalyst. Nanostructuration of carbon particles into three-dimensionally (3-D) ordered nanostructured particles is one of the most effective approaches in catalyst support development, because the architectural advantages that allow efficient transport phenomena in the PEMFC improve the electrocatalytic performance and durability at low Pt loadings.[11]

In our previous work, we prepared several ordered 3-D nanostructured materials consisting of Pt deposited on the surfaces of carbon particles (Pt/C) via spray drying, using carbon NPs as the host materials and polystyrene latex (PSL) as a template.[7,12,13] The electrocatalytic performance of the Pt/C catalyst improved when the morphology of the carbon particles was changed from dense to hollow.[7] The performance was even higher when microflower-like porous Pt/C was used.[12,13] The presence of pores on the carbon particle surfaces and the pore size influence the number of active Pt sites and the hydrodynamics through the packed catalyst. Well-ordered macroporous carbon particles cannot be prepared using the spray-drying method and carbon NPs, because the hydrophobic nature of carbon NPs is not amenable to formation of homogeneous mixtures with PSL particles.[14] Organic materials and polymers that can be converted to carbon, such as phenolic resin, are suitable for the production of carbon particles with well-ordered structures.[15] Moreover, the synthesis of carbon from phenolic resin is suitable for industrial applications because of the high production yield and inexpensive raw material.[16] Functionalization of phenolic resin for the synthesis

Additional Supporting Information may be found in the online version of this article.

Correspondence concerning this article should be addressed to R. Balgis at ratna-balgis@hiroshima-u.ac.jp and T.Ogi at ogit@hiroshima-u.ac.jp

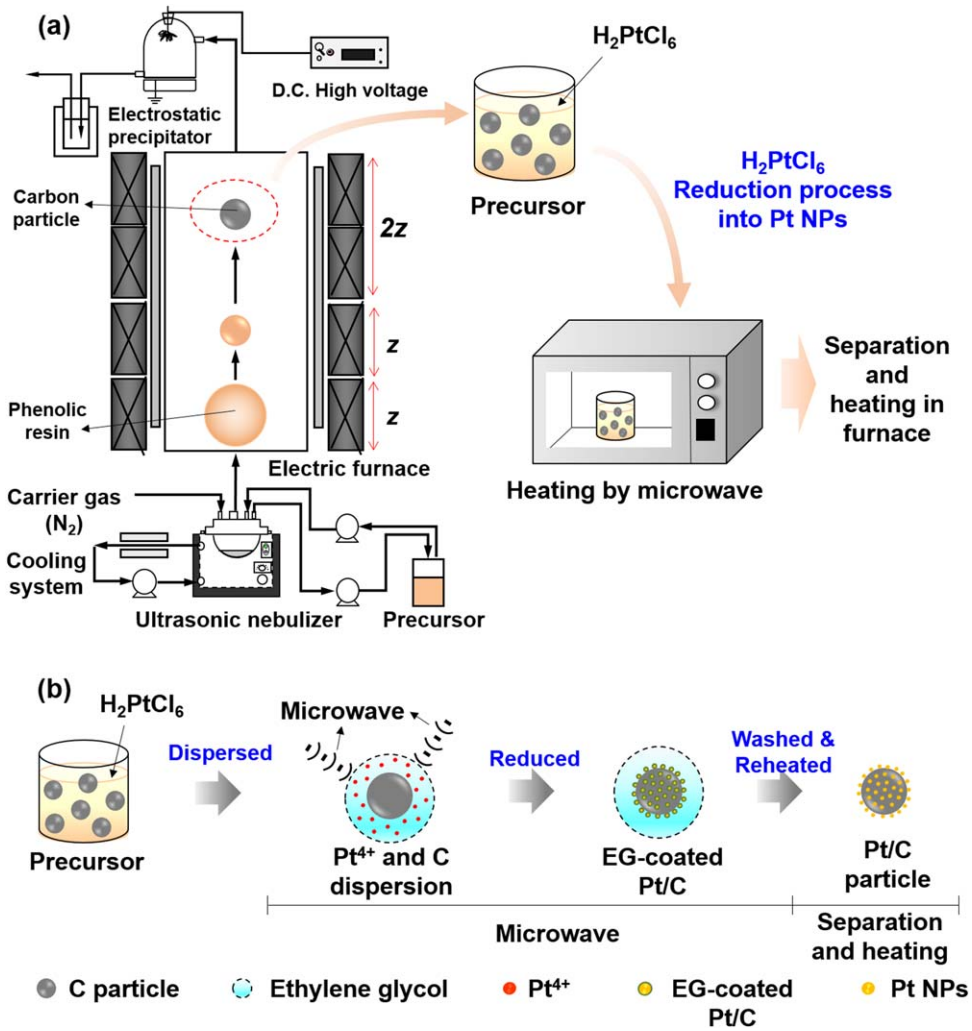

Figure 1. Schematics of (a) experimental setup and (b) Pt NP deposition process via EG-assisted MW method.

[Color figure can be viewed in the online issue, which is available at wileyonlinelibrary.com.]

of 3-D ordered carbon particles for catalyst supports is also promising, because the aromatic structures may give high electronic conductivity. However, the morphology that is appropriate for a catalyst support still needs to be determined.

In this study, we investigated how nanostructuration of a catalyst support determines the Pt deposition behavior and catalytic activity of the Pt/C catalyst. We evaluated the effects of various morphologies and pores sizes of catalyst supports on the catalytic activity in depth, because, to date, only 3-D carbon particles with nanosized to mesosized pores have been evaluated.[17,18] We also determined the best catalyst support structure for achieving higher Pt catalytic activity. A fluid dynamic approach was also used as a simple but effective tool to explain the qualitative correlation between the structure of the catalyst support and the catalytic activity. We clarified how transport phenomena affect the catalytic activity, in terms of electrochemical kinetics. The catalytic activity was qualitatively estimated by observing the flow pattern of the reactant through the catalyst support during activity tests.

Experimental

Preparation of Pt/C electrocatalysts via hybrid aerosol and microwave-assisted colloidal processes

Nanostructured NPs with various morphologies were prepared from an aqueous solution containing 0.25 wt % phenolic resin (Sumitomo Bakelite, Tokyo, Japan) and PSL particles of various sizes and with various charges, using a spray method, as described in our earlier report.[19] A tubular furnace consisting of four stacked, with same height (z) was used and set at 150°C, 300°C, 1000°C, and 1000°C from bottom to top, respectively. N_2 gas was used to carry droplets through the furnace at controlled flow rates of 0.8 L min^{-1}, as shown in Figure 1a. Positively and negatively charged PSL particles were used to control self-assembly of the phenolic resin and charged PSL particles. Hollow and porous carbon particles were obtained by fixing the mass ratio of phenolic resin to PSL particles (~230 nm in diameter) at 0.63, because this is a sufficient mass ratio to obtain completely hollow and well-structured carbon particles, as found in our previous study.[19] PSL particles of three different sizes (i.e., ~100 nm, ~230 nm, and ~300 nm) were used to adjust the pore sizes of the carbon particles.

Pt NP deposition was performed using an Microwave (MW)-assisted colloidal process, as shown in Figure 1b. The nanostructured carbon particles (10 mg) were dispersed in ethylene glycol (EG; 20 mL) by ultrasonication for 2 min. Chloroplatinic acid was added and the solution was ultrasonicated for 30 min. The solution was subjected to MW heating for 2 min in an MW-assisted organic synthesis Initiator$^+$ (Biotage, Uppsala, Sweden) operated at 150°C. The solution was cooled to room temperature, and the product was continuously

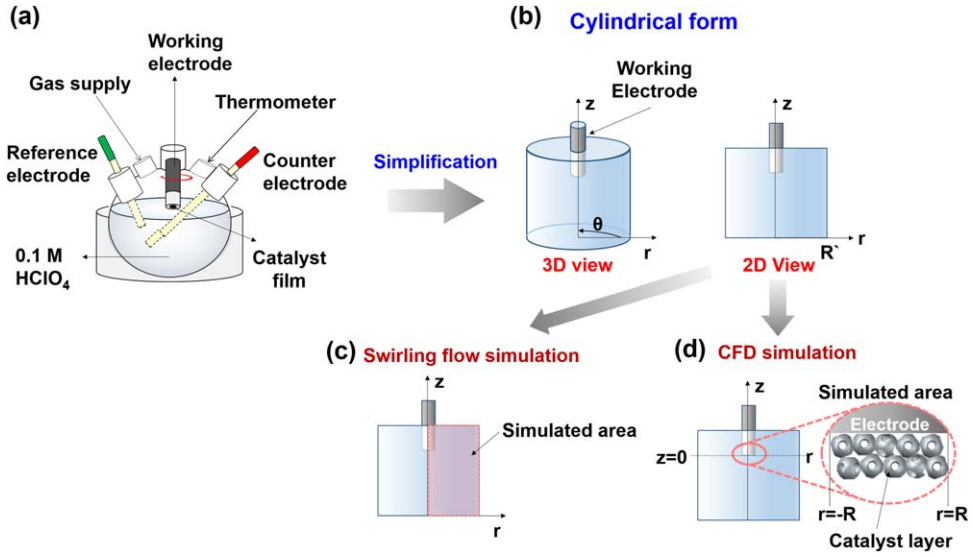

Figure 2. Schematics of (a) ORR activity test, (b) simplified ORR test chamber for fluid flow simulation, (c) simulated area for swirling flow simulation, and (d) simulated area for CFD simulation.

[Color figure can be viewed in the online issue, which is available at wileyonlinelibrary.com.]

washed with ultrapure water (300 mL) at 80°C to remove excess EG. The product was dried in a vacuum furnace at 80°C for 30 min and reheated at 200°C for 1 h in air.

Materials characterization

The zeta potentials and PSL particle sizes (D_p) of aqueous solutions containing either phenolic resin, PSL, or both were determined using a zetasizer (Zetasizer Nano ZSP, Malvern Instruments, Malvern, UK). The catalyst morphology was observed using field-emission scanning electron microscopy (SEM; S-5000, 20 kV, Hitachi High-Tech, Tokyo, Japan) and transmission electron microscopy (TEM; JEM-2010, 200 kV, JEOL, Tokyo, Japan). The amount of Pt in the catalyst was determined using inductively coupled plasma mass spectrometry (SPS-3000, Seiko Instrument, Chiba, Japan). The crystal structures of the Pt/C particles were determined using x-ray diffraction (XRD; D2 PHASER, Bruker, Billerica, MA). The surface areas of the nanostructured carbon particles were determined quantitatively by N_2 adsorption–desorption (BELSORP-max, BEL Japan, Osaka, Japan), using the Brunauer–Emmett–Teller (BET) method.

Electrochemical characterization

Electrochemical characterization was performed using cyclic voltammetry (CV) and a rotating disk electrode (HR-301, Hokuto Denko, Tokyo, Japan), as shown in Figure 2a. A reversible hydrogen electrode was used as the reference electrode for these measurements. A catalyst ink was prepared by dispersing Pt/C catalyst (5.3 g) in a mixture of ultrapure water (1.9 mL) and isopropanol (0.6 mL; Cica-reagent, Kanto Chemical, Tokyo, Japan). A Nafion® dispersion (5 wt %, 10 μL; Wako Pure Chemical Industries, Osaka, Japan) was added, and the mixture was placed in an ice bath and sonicated for about 30 min. Catalyst ink (10 μL) was transferred to a polished glassy carbon disk and allowed to dry in a chamber with controlled atmosphere, to form a thin catalyst film. The amount of Pt on the glassy carbon was 13.8 μg-Pt cm^{-2}. The amount of Pt should be in adequate range to obtain good thin film to suppress mass-transport resistance through the catalyst layer and improve the possibility for the repeatability of measurement results.[20,21] The electrochemical measurement steps and conditions used were described in our earlier publication.[7]

Model of fluid flow through nanostructured Pt/C catalyst

A computational simulation was conducted to illustrate the theoretical flow pattern of dissolved oxygen inside the catalyst layer during oxygen reduction reaction (ORR) activity tests. The simulation was performed in two steps. The first step was calculation of the electrolyte velocity on the surface of the catalyst layer, using FlexPDE 6.0. The test chamber, of radius R, was simplified and modeled using cylindrical coordinates, that is, r, θ, and z, as shown in Figure 2b. Rotation of the electrode caused an axisymmetric swirling flow inside the test chamber. In this particular case, the flow pattern in one half of the chamber can be assumed to be the same as that in the other half, therefore, only half of the chamber was simulated, as shown in Figure 2c. The effects of oxygen diffusion were assumed to be insignificant compared with those of forced convection by electrode rotation. The movement of dissolved oxygen was, therefore, mainly driven by the rotational force. Equations 1–3 were applied for swirling flow at a steady state, according to FlexPDE.

Axial momentum equation

$$\rho\left(v_r\frac{\partial v_z}{\partial r}+v_z\frac{\partial v_z}{\partial z}\right)=-\frac{\partial p}{\partial z}+\mu\left[\frac{\partial^2 v_z}{\partial r^2}+\frac{\partial^2 v_z}{\partial z^2}\right]+L_z \quad (1)$$

Radial momentum equation

$$\rho\left(v_r\frac{\partial v_r}{\partial r}+v_z\frac{\partial v_r}{\partial z}-\frac{v_\theta^2}{r}\right)+\frac{\partial p}{\partial r}=\mu\left[\frac{\partial^2 v_r}{\partial r^2}+\frac{\partial^2 v_r}{\partial z^2}-\frac{v_r}{r^2}\right]+L_r \quad (2)$$

Circumferential momentum equation

$$\rho\left(v_r\frac{\partial v_\theta}{\partial r}+v_z\frac{\partial v_\theta}{\partial z}-\frac{v_r v_\theta}{r}\right)=\mu\left[\frac{\partial^2 v_\theta}{\partial r^2}+\frac{\partial^2 v_\theta}{\partial z^2}-\frac{v_\theta}{r^2}\right]+L_\theta \quad (3)$$

ρ, μ, v, p, r, and L are the mass density, viscosity, velocity, pressure, distance from the center of the cylinder in the radial direction, and angular momentum, respectively. Subscript letters indicate the directions of the variables in cylindrical coordinates. The angular momentum represents the force caused

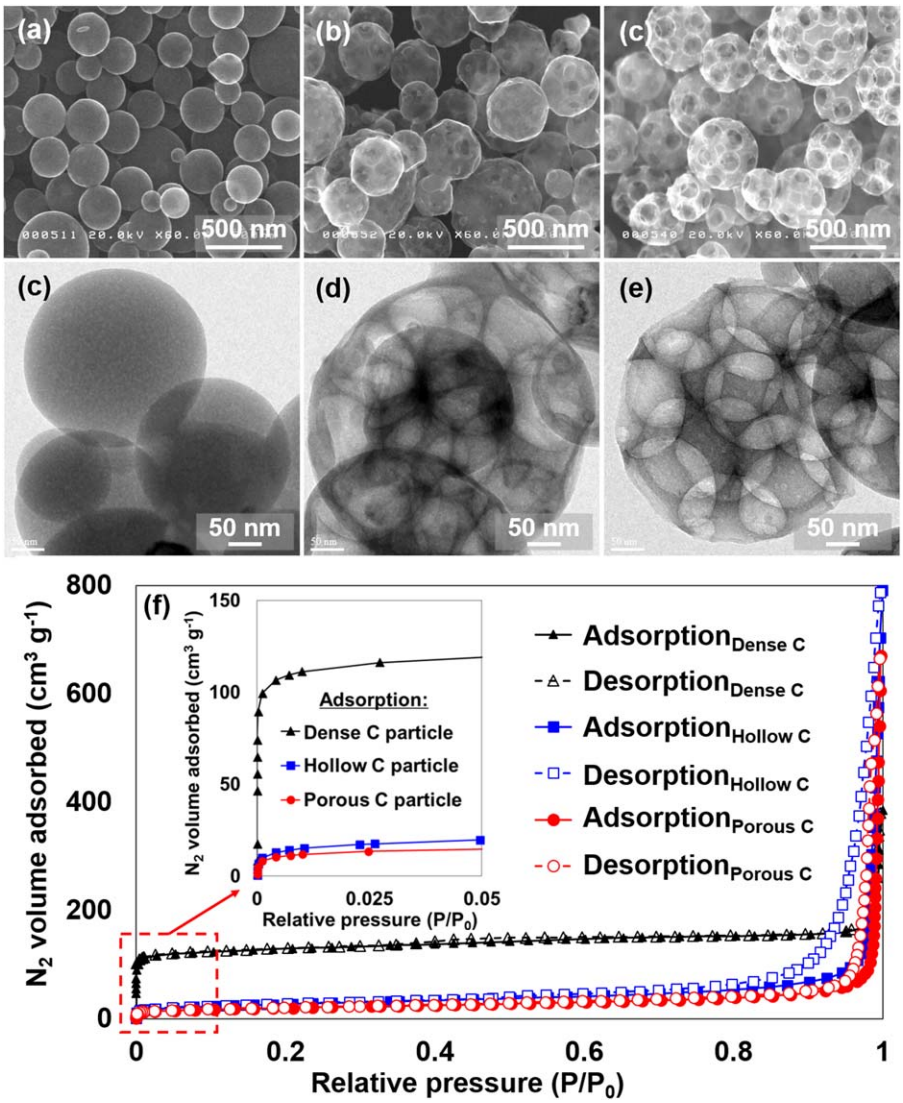

Figure 3. SEM and TEM images of (a, c) dense, (b, d) hollow, and (c, e) porous carbon particles; (f) N_2 adsorption–desorption isotherm curves of nanostructured carbon particles.

[Color figure can be viewed in the online issue, which is available at wileyonlinelibrary.com.]

by electrode rotation at an angular velocity ω, as defined in Eqs. 4–6

$$L_z = mr\omega^2 v_z \tag{4}$$

$$L_r = mr\omega^2 v_r \tag{5}$$

$$L_\theta = mr\omega^2 v_\theta \tag{6}$$

There was no slip between the electrolyte and the wall of the test chamber, therefore, v_r, v_z, and v_θ equal zero at $r = R$. The axial, radial, and circumferential velocities are assumed to be constant in the θ direction.

In the second step, the velocity distribution inside the catalyst layer was simulated using Autodesk Simulation CFD 2015. The catalyst layer was simplified to a cross-sectional view of 10 magnified catalyst particles randomly packed in two layers, as shown in Figure 2d, for better visualization of the channels between catalyst particles. The building geometry was developed and meshed using AutoCAD 2015. Three sets of catalyst were prepared and simulated separately, that is, one set of hollow catalyst and two sets of porous catalysts. The pore: particle diameter ratios of the porous catalyst sets were 0.3 and 0.5, respectively. The predicted velocity at the electrode surface obtained in the first step of the simulation was used as the inlet boundary for Eqs. 7–9.

Axial momentum equation

$$\rho\left(\frac{\partial v_z}{\partial t} + v_r\frac{\partial v_z}{\partial r} + v_z\frac{\partial v_z}{\partial z}\right) = -\frac{\partial p}{\partial z} + \mu\left[\frac{1}{r}\frac{\partial}{\partial r}\left(r\frac{\partial v_z}{\partial r}\right) + \frac{\partial^2 v_z}{\partial z^2} + \right] + \rho g_z \tag{7}$$

Radial momentum equation

$$\rho\left(\frac{\partial v_r}{\partial t} + v_r\frac{\partial v_r}{\partial r} + v_z\frac{\partial v_r}{\partial z} - \frac{v_\theta^2}{r}\right) = -\frac{\partial p}{\partial r} + \mu\left[\frac{\partial}{\partial r}\left(\frac{1}{r}\frac{\partial}{\partial r}(rv_r)\right) + \frac{\partial^2 v_r}{\partial z^2}\right] + \rho g_r \tag{8}$$

Circumferential momentum equation

$$\rho\left(\frac{\partial v_\theta}{\partial t} + v_r\frac{\partial v_\theta}{\partial r} + v_z\frac{\partial v_\theta}{\partial z} - \frac{v_r v_\theta}{r}\right) = \mu\left[\frac{\partial}{\partial r}\left(\frac{1}{r}\frac{\partial}{\partial r}(rv_\theta)\right) + \frac{\partial^2 v_\theta}{\partial z^2}\right] + \rho g_\theta \tag{9}$$

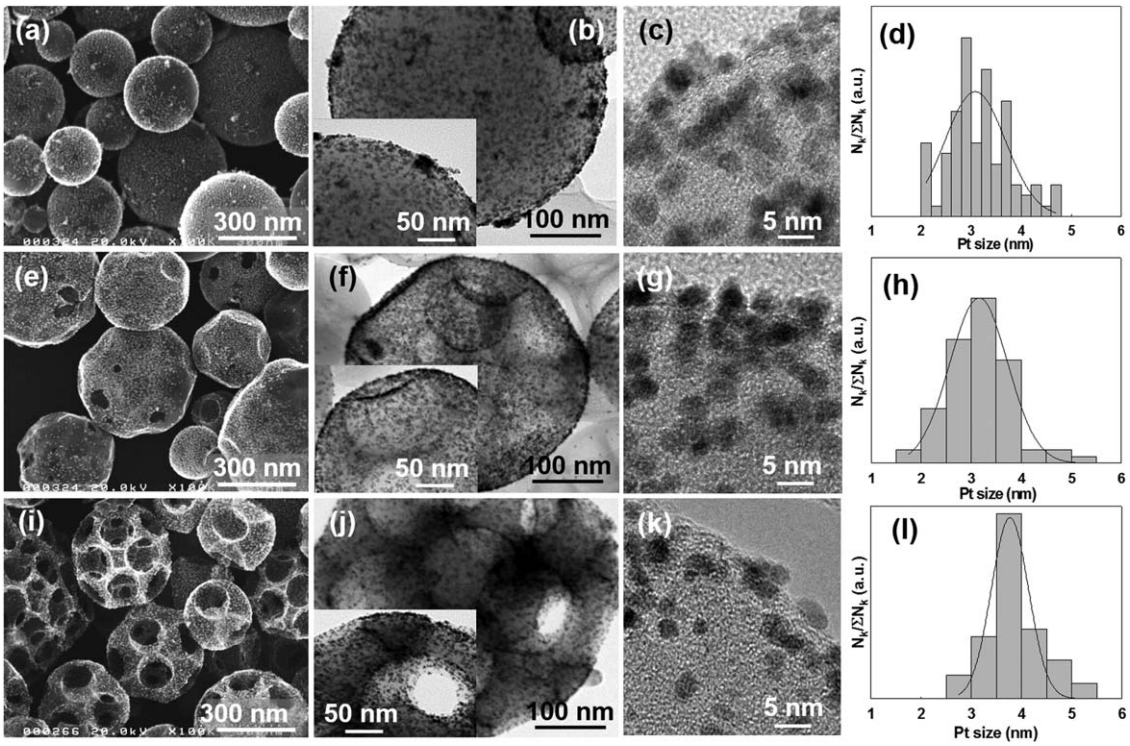

Figure 4. SEM, TEM, and high-resolution TEM images and histogram of Pt NP size distributions for (a–d) Pt/C_{dense}, (e–h) Pt/C_{hollow}, and (i–l) Pt/C_{porous} catalysts.

Oxygen diffusion in the electrolyte obeyed Fick's law. The continuity equation, Eq. 10, was used to simulate the oxygen transport.

$$\rho\left(\frac{\partial X}{\partial t}+v_r\frac{\partial X}{\partial r}+\frac{v_\theta}{r}\frac{\partial X}{\partial \theta}+v_z\frac{\partial X}{\partial z}\right) = \rho D_{O_2}\left[\frac{1}{r}\frac{\partial}{\partial r}\left(r\frac{\partial X}{\partial r}\right)+\frac{1}{r^2}\frac{\partial^2 X}{\partial \theta^2}+\frac{\partial^2 X}{\partial z^2}\right] \tag{10}$$

Where X, ρ, and D_{O_2} are the mass fraction, mass density, and diffusivity of oxygen, respectively. Oxygen was supplied to the catalyst at a constant concentration and the pressure at $r = R$ and $r = -R$ were set as atmospheric. The dissolved oxygen concentration at the inlet boundary was calculated based on Henry's law. It was assumed that the Pt particle size was homogeneous in all cases.

Results and Discussions

Nanostructuration of carbon particles for catalyst support

Spray pyrolysis of an aqueous solution containing phenolic resin resulted in the formation of dense spherical carbon particles. The morphology of the carbon particles was tuned by adding controllable charged PSL particles as a template. The addition of positively charged PSL created an attractive force with the negatively charged phenolic resin, and PSL–phenolic resin with a core–shell structure was formed. The addition of negatively charged PSL created a repulsive force with the negatively charged phenolic resin, which made both particles move independently in the droplets.[14] Figure 3 shows the various carbon particle morphologies after nanostructuration. Spray pyrolysis of the phenolic resin gave spherical dense carbon particles, as shown in Figure 3a. The addition of positively and negatively charged PSL particles resulted in hollow and porous carbon particles, as shown in Figures 3b, c, respectively; this is consistent with our previous work.[14,19] The morphologies of the obtained carbon particles were confirmed using TEM. Figure 3c shows the formation of a completely spherical and dense morphology. Macropores covered by thin shells of carbon are clearly observed in Figure 3d; this confirms the formation of a hollow morphology. Figure 3e shows the formation of macropores inside and on the surfaces of carbon particles.

The structural properties of the obtained carbon particles were evaluated using N_2 adsorption–desorption measurements; the isotherm curves are shown in Figure 3f. The isotherm curves show an initial rapid rise in the adsorbed gas volume with increasing relative pressure, followed by a slow increase, that is, type II isotherm curves. The inset in Figure 3f shows the inflection point corresponding to both completion of monolayer coverage and pore filling by capillary condensation. It can be seen that dense carbon particle adsorbed the highest volume of N_2, followed by hollow and porous carbon particles, respectively, indicating that the dense carbon particles had larger amounts of micropores than did the hollow and porous carbon particles. The isotherm curve of the dense carbon particles shows no hysteresis, whereas that of the hollow carbon particles shows type C hysteresis, which was identified by de Boer as indicating a mixture of tapered or wedge-shaped pores with open ends.[22] In contrast, the porous carbon curve shows type A hysteresis, which is principally caused by cylindrical pores open at both ends.[22] The specific surface areas (S_{BET}) of the particles were calculated to be 490.7 $m^2\ g^{-1}$, 95.8 $m^2\ g^{-1}$, and 69.9 $m^2\ g^{-1}$ for dense, hollow, and porous carbon particles, respectively.

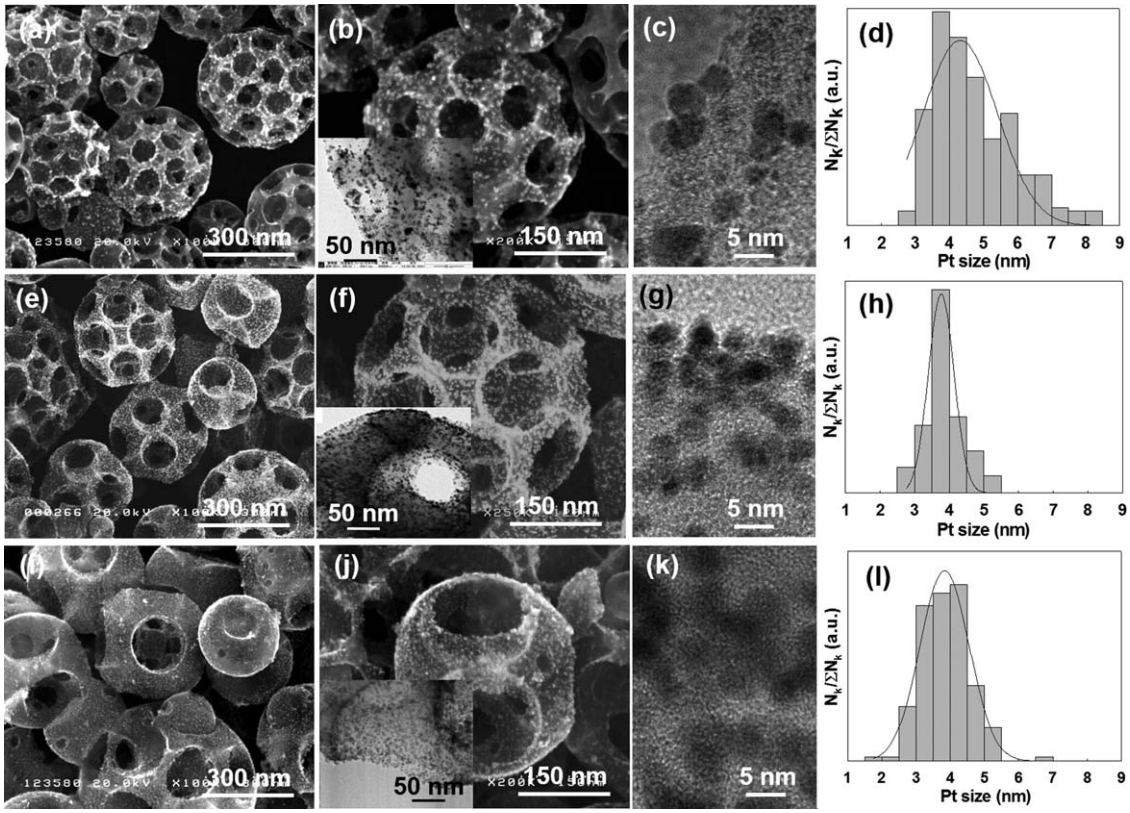

Figure 5. SEM, TEM, and high-resolution TEM images and histogram of Pt NP size distributions for Pt/C_{porous} catalysts with pore sizes of (a–d) 85 nm, (e–h) 120 nm, and (i–l) 165 nm.

Morphologies and crystallinities of nanostructured Pt/C catalysts

The aim of this work was to investigate the effects of structural engineering of the catalyst support on the activity of the Pt catalyst. The configuration of the catalyst support structure is critical for effective gas/water diffusion and proton/electron transport to and from the catalytic sites without sacrificing sites for Pt deposition. In this study, carbon particles with three different morphologies, namely dense, hollow, and porous, were used. They were synthesized using an aerosol spray pyrolysis process, as described elsewhere.[19]

Functionalization of the nanostructured carbon particles was performed by Pt deposition (~15 wt %) on the nanostructured carbon surfaces, with mediation by EG, using an MW method, as shown in Figure 1b. Pt^{4+} from chloroplatinic acid and nanostructured carbon particles were dispersed in EG, which acted as a solvent, a binder, and a Pt-ion reducing agent. The Pt ions were well dispersed in EG; after reduction, they were deposited on the surfaces of the nanostructured carbon particles. The MWs transferred heat evenly into the precursor up to 150°C, which can accelerate reduction of Pt. The entire surface of the nanostructured carbon particle soon became well decorated with uniform-sized Pt NPs. The growth of Pt NPs was restrained by the presence of EG as a binder. The EG that remained on the surfaces of the Pt NPs was removed using high-temperature ultrapure water, so that it did not affect the Pt/C catalyst.

Figure 4 shows SEM and TEM images of the nanostructured Pt/C catalysts. The figure shows that Pt NPs were deposited on the surfaces of the dense and hollow carbon particles. The Pt NPs were well dispersed, although some Pt agglomeration was observed, as shown in Figures 4a–g. The TEM images in Figure 4b confirm the formation of Pt islands in some parts of the dense carbon particles. Less Pt agglomeration was observed on the hollow carbon particles, as shown in Figure 4f, and use of the porous carbon particles led to agglomeration-free Pt NPs, as shown by the SEM and TEM images in Figures 4i, j.

The high-resolution TEM images in the insets of Figures 4b, f, j indicate that Pt NPs were also deposited on the inner surfaces of the porous carbon particles, and even in cavities. The open macropores on the carbon particle surfaces probably provide paths for Pt NPs to pass through the exterior and become deposited on the inner surfaces of the carbon particles. Conversely, we observed that the freshly reduced Pt NPs could not penetrate into the pores of neither dense carbon nor hollow carbon. Probably because of the pore size was smaller than the Pt size or the barriers formed on the pore surfaces obstructed the entrances. However, once the Pt NPs were able to penetrate the surface barriers, it was possible for the Pt NPs to be dispersed on the surfaces of the inner pores, which were larger. Those theories explain the formation of agglomerated Pt NPs on some surface of both dense and hollow carbon particles. In contrast to the micropores and mesopores, rejection on the macropore surfaces was much lower especially when it was helped with appropriate speed of stirring. The Pt NPs were, therefore, able to penetrate easily into the pores and cavities, as a result of EG flow. Histograms of the size distributions of the Pt NPs on the surfaces of dense, hollow, and porous carbon particles are shown in Figures 4d, h, l, respectively, and the average sizes are about 3.2 nm, 3.2 nm, and 3.9 nm, respectively.

To deepen our understanding of the effects of Pt NP deposition on the surfaces of porous carbon particles, three pore

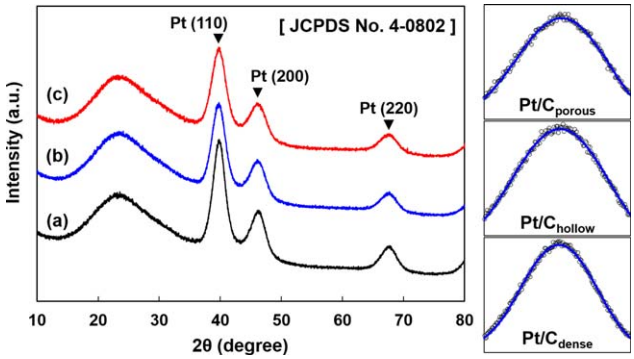

Figure 6. XRD patterns of Pt/C catalysts: (a) dense, (b) hollow, and (c) porous, with pore sizes of 120 nm.

[Color figure can be viewed in the online issue, which is available at wileyonlinelibrary.com.]

sizes, that is, 85 nm, 120 nm, and 165 nm, were examined. Figure 5 shows that Pt NP dispersion improved with increasing pore size. The Pt NPs were agglomerated and localized on some of the carbon particles with a pore size of 85 nm, as shown in Figure 5b, but well dispersed on the surfaces of carbon particles with pore sizes of 120 nm and 165 nm (Figures 5f, j, respectively). These results emphasize that Pt NP dispersion is affected not only by the morphology but also by the pore size of the catalyst support. The Pt NP sizes calculated from the high-resolution TEM images for more than 250 NPs were about 4.7 nm, 3.9 nm, and 3.9 nm for Pt/C with pore sizes of 85 nm, 120 nm, and 165 nm, respectively; the histograms are shown in Figures 5d, h, l, respectively.

The XRD patterns of the dense, hollow, and porous Pt/C particles are shown in Figure 6. A broad peak at around 2θ 25°, corresponding to the diffraction of carbon black, is observed in all the XRD patterns. Pt diffraction peaks are clearly observed for all particles, at 2θ 39°, 46°, and 68°, corresponding to the (111), (200), and (220) crystal planes, respectively (JCPDS card No. 4-0802). The crystallite sizes of the Pt NPs, calculated using the Scherrer equation, were 2.5, 2.3, and 2.2 for dense, hollow, and porous Pt/C, respectively. The crystallite sizes of the Pt NPs were slightly smaller than the diameters calculated from the TEM images. This indicates aggregation of Pt crystals, although some Pt particles grew individually.

Electrocatalytic activities of nanostructured Pt/C catalysts

The electrochemical characteristics of the prepared Pt/C catalysts were investigated based on CV and ORR polarization curves obtained under the same measurement conditions.

Figure 7a shows the CV adsorption–desorption characteristics of the dense, hollow, and porous Pt/C catalysts. For the prepared Pt/C catalysts, a weak hydrogen ion adsorption peak in the potential range of 0.31–0.13 V for dense and hollow Pt/C and 031–0.13 V for porous Pt/C catalysts; and a strong adsorption peak located between 0.13 V and 0.02 V were observed during reverse potential scanning, and were assigned to weakly and strongly bonded hydrogen atoms, respectively. Pt/C_{hollow}, and Pt/C_{porous} show the typical voltammograms of Pt/C, however Pt/C_{dense} has a very broad peak at a potential range of 0.7 V–0.4 V showing that it has a high pseudocapacitance. The electrochemical surface area (ECSA) of Pt in the working electrode was calculated using the hydrogen adsorption charge ($Q_{H\text{-adsorption}}$) limited by the minimum potential, which was selected to be just above the potential of H_2 generation (between 0.3 V and ~0.06 V for dense Pt/C; and 0.4 V and ~0.06 V for hollow and porous Pt/C). The corresponding desorption peaks were observed during the reverse potential scan. The average of calculated ECSAs were 53.4 $m^2\ g^{-1}$, 72.8 $m^2\ g^{-1}$, and 107.4 $m^2\ g^{-1}$-Pt for the Pt/C_{dense}, Pt/C_{hollow}, and Pt/C_{porous} catalysts, respectively. The ECSA value of the Pt/C_{dense} catalyst was lower than that of Pt/C_{hollow}, and that of the Pt/C_{porous} catalyst was highest, almost twice those of the other catalysts. In addition to the effect of Pt agglomeration, which is probably not the major factor, this ECSA value might be affected by the distance between Pt NPs. The external surface area calculated from N_2 adsorption desorption analysis were about 15.4 $m^2\ g^{-1}$, 64.4 $m^2\ g^{-1}$, and 41.3 $m^2\ g^{-1}$ for dense, hollow, and porous carbon particles, respectively. Dense carbon particle has the smallest active site for Pt NPs to deposit and make the distance between Pt NPs becomes shorter than those on hollow and porous carbon. Therefore, only Pt surfaces that do not face each other were active. Hollow carbon particle has the highest external surface area but the interconnected bimodal pore system of the porous structure may lengthen the distance among Pt NPs and suppressed the possibility of Pt migration which would increase the Pt NP active surface area.

Typical oxygen reduction polarization curves for the Pt/C_{dense}, Pt/C_{hollow}, and Pt/C_{porous} catalysts, recorded after 50 CV cycles at a rotation speed of 1600 rpm, are shown in Figure 7b. At an electrode angular speed of 1600 rpm, the diffusion-limiting current density for materials that support direct four-electron transfer, that is, Pt-based electrodes, usually ranges between −5 and −6 mA cm^{-2}, and can be reached by those three morphologies of the Pt/C catalysts. The ORR activity tests were performed at different rotation speeds (i.e., 400 rpm, 900 rpm, 1600 rpm, 2500 rpm, and 3600 rpm) to obtain Koutecký–Levich plots, shown in Figure 7c. The number of electrons involved in the ORR was calculated using the Koutecký–Levich equation[23]; four electrons were involved for all morphology of the Pt/C catalysts. Figure 7d shows the ORR curves of Pt/C porous catalyst at various rotation speeds. The inset of Figure 7d shows that half-wave potential ($E_{1/2}$, the point half way between zero current and the diffusion-limited current density plateau J_{lim}) was around 0.88 V. Therefore, the target potential for calculation of the mass activities was determined at slightly higher than $E_{1/2}$, at $E = 0.9$ V. The Pt mass activity (MA) values were calculated by normalizing the Pt loading on the disk electrode. The Pt/C_{porous} catalyst showed the highest mass activity about 265.6 mA mg^{-1}-Pt, followed by Pt/C_{hollow} and Pt/C_{dense} which were about 259.5 and 241 mA mg^{-1}-Pt, respectively. The summary of electrocatalytic activities (ECSA and MA) were shown in Figure 7e. Pt/C_{dense} catalyst has the smallest MA which can be attributed to partial blocking of active catalytic sites, probably by microbubbles formed by cavitation during the ORR activity test. As previously mentioned, the Pt/C_{dense} catalyst had only micropores and mesopores. The microbubbles probably blocked some of the micropores, which would significantly affect the hydrodynamics of the Pt/C_{dense} catalyst. The microbubbles remained unbroken because of the strong convective force in the axial direction at high angular velocities. In addition, low charge transfer as a result of the low overpotential (η) is suspected to contribute to microbubble preservation.

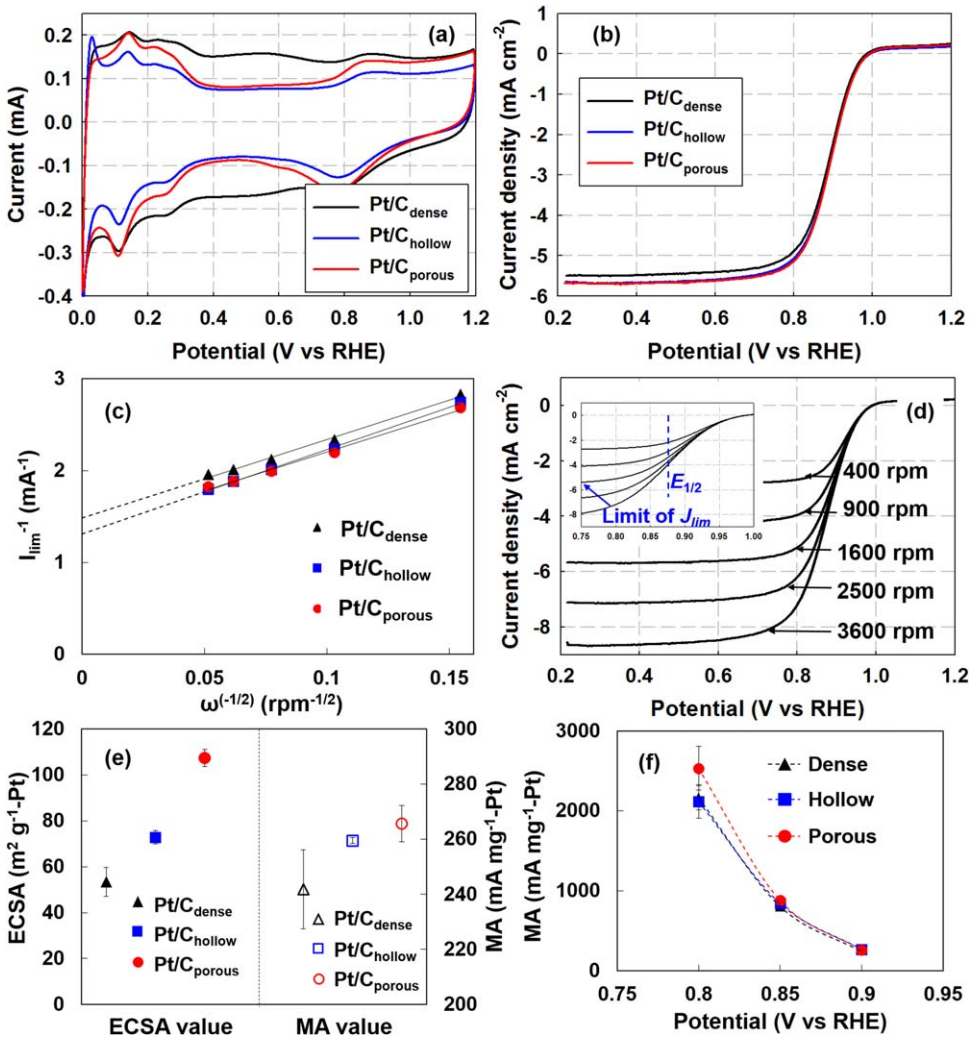

Figure 7. (a) CV of Pt/C_{dense}, Pt/C_{hollow}, and Pt/C_{porous} catalysts after 50 cycles in oxygen-free 0.1 M $HClO_4$ (cycling between 0 and 1.2 V at sweep rate of 50 mV s^{-1}), (b) comparison of ORR polarization curves of Pt/C_{dense}, Pt/C_{hollow}, and Pt/C_{porous} catalysts at rotation rate of 1600 rpm after 50 cycles in oxygen-saturated 0.1 M $HClO_4$ at sweep rate of 10 mV s^{-1}, (c) Koutecký–Levich plots for Pt/C_{dense}, Pt/C_{hollow}, and Pt/C_{porous} catalysts at various rotation rates and potential of 0.9 V, (d) ORR polarization curves of Pt/C_{porous} catalysts at different rotation rates, (e) ECSA and MA values at $E = 0.9$ V, and (f) MA values at various E.

[Color figure can be viewed in the online issue, which is available at wileyonlinelibrary.com.]

Mass activity of prepared samples was calculated at E, 0.8 V, 0.85 V, and 0.9 V as shown in Figure 7f. It is shown that Pt/C_{porous} catalyst has the highest value at all E. These results suggest that the morphology of the carbon catalyst support plays a crucial role in the electrocatalytic performance. The relationship between the carbon morphology and active catalytic sites can be explained based on a fluid flow model, as discussed in the Model of fluid flow around nanostructured Pt/C catalyst subsection.

Effects of Pt/C catalyst pore size on electrocatalytic activity

Understanding that a porous morphology improves the catalytic performance is important, but knowing the most appropriate pore size for achieving a superior catalytic performance is also vital. Based on this idea, the electrocatalytic activities of Pt/C catalysts with pore sizes of 85 nm, 120 nm, and 165 nm were evaluated. Figure 8a shows the CV adsorption–desorption characteristics of three porous Pt/C catalysts. It should be noted that broad peaks were observed between 0.3 V and 0.7 V in both the forward and reverse potential scans for the catalyst with a pore size of 85 nm and 165 nm, probably because of unpredictable pore formation inside the carbon particles. It was difficult for Pt to reach and be deposited on these pores, but they actively stored charge, resulting in a high pseudocapacitance. Among these curves, that for Pt/C with a pore size of 120 nm shows the clearest and greatest Pt–H adsorption and H_2 evolution peaks. The ECSA was calculated to be 50.3 $m^2\ g^{-1}$, 107.4 $m^2\ g^{-1}$, and 64.6 $m^2\ g^{-1}$-Pt for pore sizes of 85, 120, and 165, respectively. The highest ECSA was obtained at a pore size of 120 nm, showing that appropriate contacts among the gas fuel, catalyst, and membrane were obtained at this pore size. The ECSA value of Pt/C with a pore size of 85 nm was extremely low, even lower than that of dense Pt/C, probably because the carbon support predominantly acted as a charge store.

Figure 8b shows the oxygen reduction polarization curves after 50 CV cycles at a rotation speed of 1600 rpm. All three

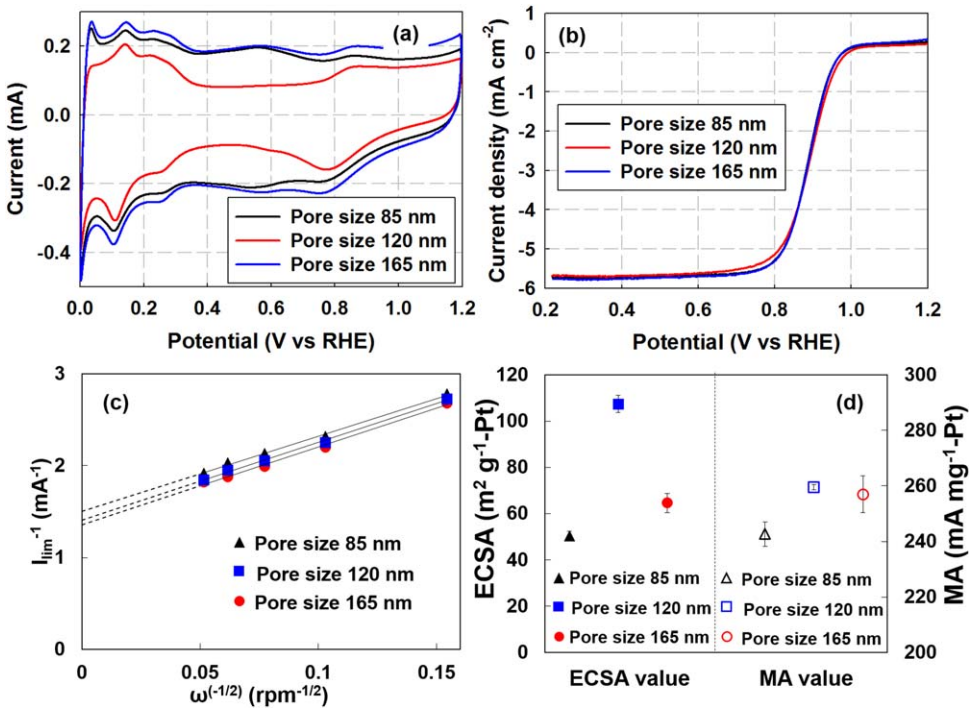

Figure 8. (a) CV of Pt/C_{porous} catalysts with pore sizes of 85, 120, and 165 nm after 50 cycles under the same measurement conditions as in Figure 7, (b) comparison of ORR polarization curves of Pt/C_{porous} catalysts with pore sizes of 85, 120, and 165 nm at a rotation rate of 1600 rpm after 50 cycles, (c) Koutecký–Levich plots of Pt/C_{porous} catalysts with pore sizes of 85, 120, and 165 nm at various rotation rates and potential of 0.9 V, and (d) ECSA and MA values of Pt/C_{porous} catalysts with pore sizes of 85, 120, and 165 nm at $E = 0.9$ V.

[Color figure can be viewed in the online issue, which is available at wileyonlinelibrary.com.]

catalysts show similar diffusion-limited current density plateaus. The Koutecký–Levich plots of catalysts which show similar slope are shown in Figure 8c and were used to calculate the mass and specific activities. The mass activity values quantified at $E = 0.9$ V for pore sizes of 85 nm, 120 nm, and 165 nm were about 242.6 mA mg^{-1}, 259.5 mA mg^{-1}, and 256.9 mA mg^{-1}-Pt, respectively. Even though the mass activity of different pores are not much different, but the ECSA are totally different as summarized in Figure 8d. It shows that at a certain size of pores, overall electocatalytic activity can be optimized by optimizing the amount of active Pt catalyst as well as minimize the pseudo capacitance ability.

Model of fluid flow around nanostructured Pt/C catalyst

The flow pattern inside the catalyst layer at an electrode angular velocity of 3600 rpm was determined using FlexPDE. At this electrode velocity, the velocity of the fluid entering the catalyst layer was 6×10^{-3} m s^{-1}. Rotation of the electrode resulted in a swirling flow pattern in the test chamber, as shown in Figure 9 for half of the test chamber. The oxygen fraction in the catalyst layer was calculated to be 4.4×10^{-5}, based on Henry's law. The flow pattern and oxygen concentration were used for computational fluid dynamic (CFD) simulation using Autodesk CFD 2015 to show the effects of the pore size on the velocity and oxygen concentration distribution between particles in the catalyst layer. A concentration fraction of 1.0 was set in the CFD simulation to represent an oxygen concentration of 4.4×10^{-5}. The analysis was based on the assumption that Pt NPs of the same size are well distributed on the catalyst support. The ability of the Pt catalyst to adsorb oxygenated species was, therefore, assumed to be homogenous.[24] The CFD simulation results for various nanostructures are shown in Figures 10a–f. The velocity and oxygen concentration profiles are represented by color gradients.

Figure 10a shows the velocity distribution of hollow particles in the packed catalyst. The velocity distribution was inhomogeneous with many stagnant areas, indicated by dark blue. The stagnant areas were particularly concentrated inside the hollows, indicating that the mesopore size was insufficient to allow unhindered flow of the electrolyte into the hollows. Oxygen transport into the hollows would then rely on diffusion only, which is very sluggish compared with convection. As a consequence, the area with stagnant flow had a very low oxygen concentration, indicated by dark blue in Figure 10b.

The absence of convective flow in some areas affected the reaction on the catalyst surface. In such areas, the electrochemical reaction was controlled only by oxygen diffusion. As a consequence, the ORR rate would not exceed the rate of oxygen diffusion to the catalyst surface. In terms of electrochemical kinetics, the current density from the reaction would be equal to the limiting current density, J_{lim}.[25] We are focusing on microscopic-scale diffusion, and, therefore, the surface of the catalyst is regarded as planar. The correlation between J_{lim} and the oxygen concentration is described by Eq. 10

$$J_{lim} = nFm_oC_o \tag{11}$$

n, F, m_o, and c_o denote the number of electrons, Faraday constant, mass-transfer coefficient, and oxygen concentration in the bulk solution, respectively. The mass-transfer coefficient is

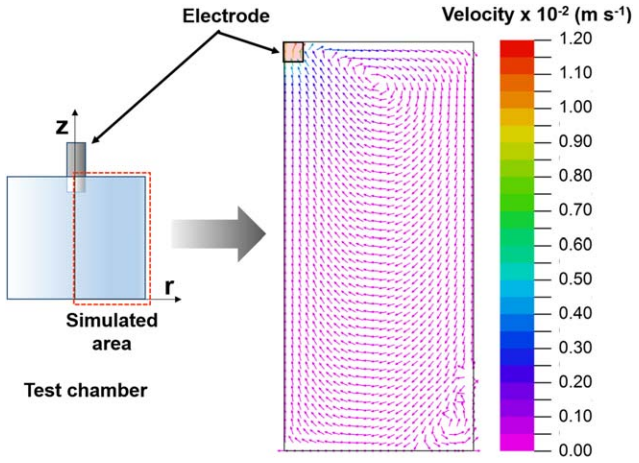

Figure 9. Swirl flow pattern in cross-sectional view of half of ORR activity test chamber. This image is reproduced from the FlexPDE 6.0 simulation.

[Color figure can be viewed in the online issue, which is available at wileyonlinelibrary.com.]

defined as the ratio between the diffusivity coefficient and the thickness of the Nernst diffusion layer. Since there was almost no oxygen deployment by convection, the oxygen concentration in the stagnant area tended to be low and decreased over time as the oxygen was consumed by ORR. The decreasing oxygen concentration furthermore resulted in the lower current density (Figure SI 1 in the Supporting Information). In the overall system, this is observed as a low ECSA. The limiting current, however, may not be observed in the catalyst polarization measurements, because it occurs locally.

Figure 10c shows the velocity distribution in the packed catalyst with a pore: particle diameter ratio of 0.3. The velocity distribution was much more homogeneous than that in the hollow particles, although many stagnant areas were still present. The pore size was not large enough to create perfect channels inside the structure, therefore, the electrolyte flow was obstructed by the catalyst wall in some areas. The sluggish diffusion of oxygen in the absence of convective flow resulted in a low oxygen concentration in that particular area, as seen in Figure 10d.

When particles with larger pores were used as the catalyst, the pores were interconnected, although the particles were randomly packed, as shown in Figure 10e. The interconnected pores created channels that allowed the fluid to pass through the particles with fewer obstacles, resulting in a better velocity distribution. The stagnant area in Figure 10e is smaller than that in Figure 10c, because of the larger pores. As a result of better convective flow, oxygen transfer to the electrode surface was more effective, indicated by smaller blue areas in Figure 10f. In this case, the reaction rate only depends on the activation overpotential, in accordance with the Butler–Volmer equation. Despite the good transport phenomena, excessively large pores in a catalyst may be disadvantageous because the surface area of the catalyst decreases and the catalyst tends to be brittle.

Conclusion

The electrocatalytic performances of nanostructured Pt/C catalysts were comprehensively evaluated. The effects of the catalyst support morphology (i.e., dense, hollow, and porous) and pore size on the electrocatalytic performance were studied. It was clearly found that the performance of the porous carbon Pt/C catalyst was the best among those of the three

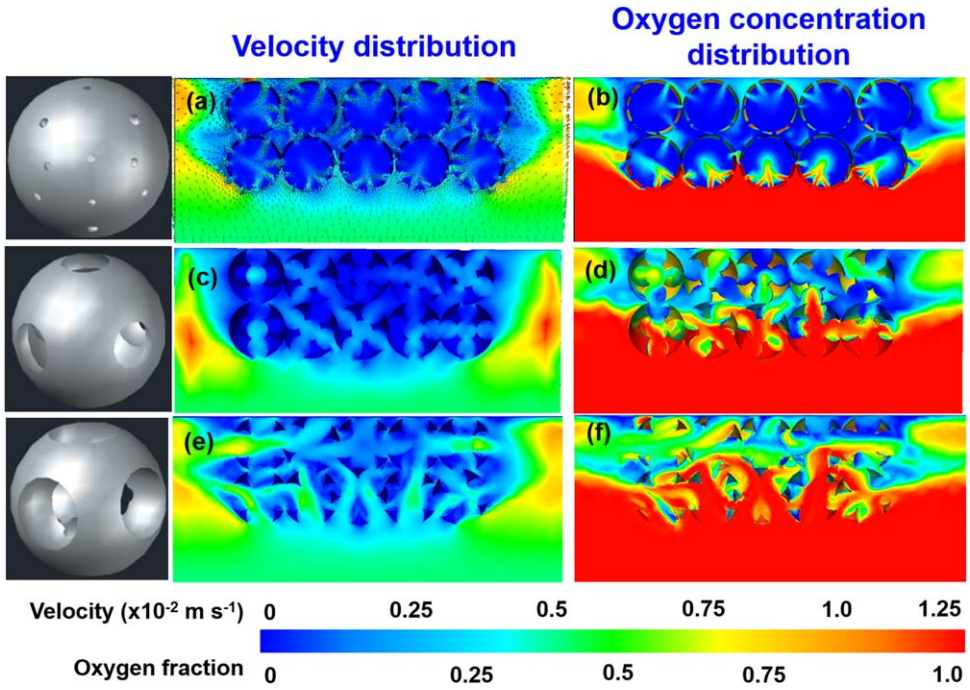

Figure 10. Velocity distribution profile in the catalyst layer consisting of (a) hollow carbon particles and porous carbon particles at a pore: particle diameter ratio of (c) 0.3 and (e) 0.5.

The corresponding oxygen concentration profile for each type of catalyst is shown in (b), (d), and (f), respectively. Outward appearance of the 3-D model of each particle is shown on the left-hand side. [Color figure can be viewed in the online issue, which is available at wileyonlinelibrary.com.]

types of catalyst, probably because of the presence of interconnected pores, which allowed better oxygen transport to the catalyst surface. Furthermore, good oxygen transport promoted effective charge transfer and consequently increased the active surface area of the catalyst. These phenomena were confirmed by fluid dynamic simulations, which were analyzed in terms of electrochemical kinetics. These results prove the effectiveness of the fluid dynamic approach in qualitatively estimating the electrocatalytic performance by observing hydrodynamic phenomena within the catalyst layer.

Acknowledgments

This research was supported by a Grant-in-Aid for Young Scientists A (26709061) and B (15K182570A) sponsored by the Ministry of Education, Culture, Sports, Science, and Technology of Japan. The authors would like to thank Dr. Eishi Tanabe from the Hiroshima Prefectural Institute of Industrial Science and Technology for helping with the TEM analysis and the Sumitomo Bakelite Co., Ltd., for supplying the phenolic resin.

Literature Cited

1. Aricò AS, Bruce P, Scrosati B, Tarascon JM, Van Schalkwijk W. Nanostructured materials for advanced energy conversion and storage devices. *Nat Mater*. 2005;4:366–377.
2. Candelariaa SL, Shao Y, Zhou W, Li X, Xiao J, Zhang J-G, Wang Y, Liu J, Li J, Cao G. Nanostructured carbon for energy storage and conversion. *Nano Energy*. 1;2012:195–220.
3. Mayrhofer KJJ, Strmcnik D, Blizanac BB, Stamenkovic V. Arenz M, Markovic NM. Measurement of oxygen reduction activities via the rotating disc electrode method: from Pt model surfaces to carbon-supported high surface area catalysts. *Electrochim Acta*. 2008;53:3181–3188.
4. Service RF. Shrinking fuel cells promise power in your pocket. *Science*. 2002;296:1222–1224.
5. Stamenkovic V, Mun BS, Mayrhofer KJJ, Ross PN, Markovic NM, Rossmeisl J, Greeley J, Nørskov JK. Changing the activity of electrocatalysts for oxygen reduction by tuning the surface electronic structure. *Angew Chem*. 2006;118:2963–2967.
6. Balgis R, Sago S, Anilkumar GM, Ogi T, Okuyama K. Self-organized macroporous carbon structure derived from phenolic resin via spray pyrolysis for high-performance electrocatalyst. *ACS Appl Mater Interfaces*. 2013;5:11944–11950.
7. Balgis R, Anilkumar GM, Sago S, Ogi T, Okuyama K. Nanostructured design of electrocatalyst support materials for high-performance PEM fuel cell application. *J Power Sources*. 2012;203: 26–33.
8. Sharma S, Pollet BG. Support materials for PEMFC and DMFC electrocatalysts-A review. *J Power Sources*. 2012;208:96–119.
9. Shao Y, Liu J, Wang Y, Lin Y. Novel catalyst support materials for PEM fuel cells: current status and future prospects. *J Mater Chem*. 2009;19:46–59.
10. Fang B, Kim JH, Kim M, Kim M, Yu J-S. Hierarchical nanostructured hollow spherical carbon with mesoporous shell as a unique cathode catalyst support in proton exchange membrane fuel cell. *Phys Chem Chem Phys* 2009;11:1380–1387.
11. Qiao Y, Li CM. Nanostructured catalysts in fuel cells. *J Mater Chem: Feature Article*. 2011;21:4027–4036.
12. Balgis R, Anilkumar GM, Sago S, Ogi T, Okuyama K. Rapid in situ synthesis of spherical microflower Pt/C catalyst via spray drying for high performance fuel cell application. *Fuel Cells*. 2012;12:665–669.
13. Balgis R, Anilkumar GM, Sago, S, Ogi T, Okuyama K. Ultrahigh oxygen reduction activity of Pt/nitrogen-doped porous carbon microspheres prepared via spray-drying. *J Power Sources* 2013;229:58–64.
14. Balgis R, Ogi T, Wang W-N, Anilkumar GM, Sago S, Okuyama K. Aerosol synthesis of self-organized nanostructured hollow and porous carbon particles using a dual polymer System. *Langmuir*. 2014;30:11257–11262.
15. Zhang S, Chen L, Zhou S, Zhao D, Wu L. Facile synthesis of hierarchically ordered porous carbon via in situ self-assembly of colloidal polymer and silica spheres and its use as a catalyst support. *Chem Mater*. 2010;22:3433–3440.
16. Ryu J, Suh Y-W, Suh DJ, Ahn DJ. Hydrothermal preparation of carbon microspheres from mono-saccharides and phenolic compounds. *Carbon*. 2010;48:1990–1998.
17. Galeano C, Meier JC, Peinecke V, Bongard H, Katsounaros I, Topalov AA, Lu A, Mayrhofer KJJ, Schüth F. Toward highly stable electrocatalysts via nanoparticle pore confinement. *J Am Chem Soc*. 2012;134:20457−20465.
18. Songa S, Liang Y, Li Z, Wanga Y, Fu R, Wub D, Tsiakaras P. Effect of pore morphology of mesoporous carbons on the electrocatalytic activity of Pt nanoparticles for fuel cell reactions. *Appl Catal B Environ*. 2010;98:132–137.
19. Balgis R, Ogi T, Arif AF, Anilkumar GM, Mori T, Okuyama K. Morphology control of hierarchical porous carbon particles from phenolic resin and polystyrene latex template via aerosol process. *Carbon*. 2015;84:281–289.
20. Garsany Y, Baturina OA, Swider-Lyons KE, Kocha SS. Experimental methods for quantifying the activity of platinum electrocatalysts for the oxygen reduction reaction. *Anal Chem*. 2010;82:6321–6328.
21. Gloaguen F, Confert P, Gamburzev S, Velev O, Srinivasan S. An evaluation of the macro-homogeneous and agglomerate model for oxygen reduction in PEMFCs. *Electrochim Acta*. 1998;43:3767–3772.
22. Lowell S, Shields JE. *Powder Surface Area and Porosity*, 3rd ed. New York: Chapman & Hall, 1991.
23. Chen J, Zhang W, Officer D, Swiegers GF, Walace GG. A readily-prepared, convergent, oxygen reduction electrocatalyst. *Chem Commun*. 2007;43:3353–3355.
24. Mayrhofer KJJ, Strmcnik D, Blizanac BB, Stamenkovic V, Arenz M, Markovic NM. Measurement of oxygen reduction activities via the rotating disc electrode method: from Pt model surfaces to carbon-supported high surface area catalysts. *Electrochim Acta*. 2008;53:3181–3188.
25. Bard AJ, Faulkner LR. *Electrochemical Methods Fundamentals and Applications*, 2nd ed. New York: Wiley, 2001.

Manuscript received May 29, 2015, and revision received Aug. 7, 2015.